Journal of Materials Chemistry A

ROYAL SOCIETY OF CHEMISTRY

PAPER

View Article Online
View Journal | View Issue

Cite this: J. Mater. Chem. A, 2025, 13, 16785

Tuning the interfacial chemistry in metal organic framework/graphene electrodes for boosting energy storage†

Shashank Sundriyal,*[a] Vishal Shrivastav,[a] Prashant Dubey,[b] Mansi,[a] Vit Kvasnička,[ac] Mahima Khandelwal,[a] Aby Cheruvathoor Poulose,[a] Radek Zbořil *[ac] and Aristides Bakandritsos *[ac]

Two-dimensional conductive metal–organic frameworks (2D-CMOFs) are emerging materials for electrochemical energy storage. However, their performance is often hindered by insulating interfaces between the CMOF particles. To address this limitation, we introduced and experimentally demonstrated the development of interfacial bridges through the coordination of the metal nodes of a nickel 2D-CMOF (2DNi) and the carboxyl groups from a densely and selectively functionalized graphene (graphene acid, GA). To achieve this, the 2DNi MOF was grown in the presence of GA at low temperatures and ambient pressure in water. The obtained 2DNiGA electrode material shows over a 100% capacitance improvement compared to electrodes synthesized under identical conditions using either unfunctionalized pristine graphene or post-synthetically added GA *via* physical mixing. In the latter case no formation of coordination bonds with the nickel nodes of the MOF is observed, confirming our initial hypothesis on the importance of the seamless interfacial bridging. Moreover, a hybrid, flexible supercapacitor using 2DNiGA as a positive and GA as a negative electrode delivers a superior gravimetric energy density of 71 W h kg^{-1} at 0.8 kW kg^{-1}. Notably, it delivers a similarly high volumetric energy density of 73.8 W h L^{-1} at 0.836 kW L^{-1}. The data indicate that the asymmetric supercapacitor compares favorably with top-tier supercapacitor electrodes, and uniquely combines superior gravimetric and volumetric energy densities. The supercapacitor is also robust, retaining more than 94% of its initial performance after 10 000 charge/discharge cycles, or when bent at 180°. The introduced concept of such tailored interfacial bridging offers broad potential for improving the properties of MOF materials in electrochemical energy storage.

Received 1st March 2025
Accepted 27th April 2025

DOI: 10.1039/d5ta01697e

rsc.li/materials-a

1 Introduction

In the pursuit of sustainable and high-performance energy storage solutions, supercapacitors are promising candidates owing to their rapid charge–discharge capabilities, long cycle life, and, in many cases, operation without reliance on critical raw materials, such as lithium and cobalt, which are essential in current battery chemistries. However, to fully harness the advantages of supercapacitors in a broad range of applications, it is necessary to identify electrode materials with substantially improved energy densities, which still fall considerably behind those of batteries.[1,2] Consequently, extensive research efforts have been dedicated to increasing the energy storage in supercapacitors, including improvements in volumetric energy density.[3–12] This has been mainly pursued by developing materials of low porosity and high packing/mass density, which leads to an unavoidable tradeoff between volumetric and gravimetric performance.[3] As a result, designing electrode materials that simultaneously deliver superior energy content in both volumetric and gravimetric terms remains a significant challenge.

The key to unlocking further advances lies in the meticulous design and integration of advanced materials,[2,13,14] such as MXenes,[4,15] porous and/or doped carbons,[16] and graphenes,[9,17] or metal–organic frameworks (MOFs).[18–21] MOFs are endowed with structural tunability, high surface area, and porosity, as well as redox properties.[22,23] However, the insulating nature of the MOF is the major issue that limits its direct usage in the energy storage applications which forces the researcher to use

[a]Regional Center of Advanced Technologies and Materials, The Czech Advanced Technology and Research Institute (CATRIN), Palacký University Olomouc, Šlechtitelů 27, 779 00 Olomouc, Czech Republic. E-mail: shashank.sundriyal@upol.cz; a.bakandritsos@upol.cz; radek.zboril@upol.cz

[b]Advanced Carbon Products and Metrology Department, CSIR-National Physical Laboratory (CSIR-NPL), New Delhi 110012, India

[c]Nanotechnology Centre, Centre for Energy and Environmental Technologies, VŠB–Technical University of Ostrava, 17. Listopadu 2172/15, 708 00 Ostrava-Poruba, Czech Republic

† Electronic supplementary information (ESI) available. See DOI: https://doi.org/10.1039/d5ta01697e

the MOF derived products.[24] Recently, Zhao *et al.* synthesized hierarchical mesoporous Se@(NiCo)Se_2 nanosheet arrays on conductive substrates using a bimetal porphyrin MOF as a template.[25] The resulting electrodes exhibited high specific capacity (240 mA h g^{-1} at 2 A g^{-1}), excellent cycling stability (83.2% retention after 5000 cycles), and superior energy density (49.4 W h kg^{-1}). Cherupurakal *et al.* synthesized Fe-doped TiO_2 *via* a MOF-derived route, yielding a cuboid morphology and enhanced electrochemical properties compared to pristine TiO_2.[26] The FeT electrode delivered a high specific capacitance of 925 F g^{-1} and retained 67% of its capacity after 6000 cycles. Similarly, Hu *et al.* synthesized a coral-like CNF@c-$CoSe_2$/C composite using electrostatic spinning and a wet chemical method.[27] The structure improved Na^+ diffusion, leading to high rate capability (266.5 mA h g^{-1} at 5.0 A g^{-1}) and excellent cycling stability (268.3 mA h g^{-1} after 100 cycles at 1.0 A g^{-1}). Recently, 2D MOFs have attracted significant attention due to their unique properties compared to 3D structures, including, but not limited to, the high surface to volume ratio and highly exposed metal/organic functional sites. For instance, Han *et al.* developed a novel "hard" emulsion-induced interface superassembly strategy to synthesize 2D hierarchically porous UiO-66-NH_2 nanosheets with controllable thickness and tunable meso-/microporosity.[28] This approach transforms oil-in-water emulsions into 2D solid templates, enabling the loose packing and interfacial assembly of mesostructured MOF nanounits. The resulting nanosheets exhibited superior catalytic performance in CO_2 cycloaddition reactions compared to conventional MOFs.

Recent advances in MOFs have expanded the design toolbox towards conductive MOFs (CMOFs),[29,30] addressing a major limitation related to their insulating nature. The intrinsic conductivity in CMOFs is generated by installing redox-active 2D organic linkers, like HAB (hexaaminobenzene), HITP (hexaiminotriphenylene), HHTP (hexahydroxytriphenylene) and HATP (hexaaminotriphenylene), in combination with metal ions possessing multivalence states.[31,32] 2D variants of CMOFs (2D-CMOFs) offer further advantages, particularly in terms of electron mobility and ion diffusion. In the first report on 2D-CMOF for supercapacitors, $Ni_3(HITP)_2$ was studied without carbon additives, showing a very high areal capacitance (normalized by the surface area of the material according to N_2 sorption), and with gravimetric and volumetric capacitance reaching 70 F g^{-1} and 42 F cm^{-3}, respectively, at 1 A g^{-1}.[33] The $Ni_3(HITP)_2$ 2D-CMOF studied later in symmetric cells without conductive additives delivered a gravimetric energy density of 45 W h kg^{-1} (at ~0.7 kW kg^{-1} and (100 °C), or volumetric energy density of 35 W h L^{-1}.[34] The $Cu_3(HHTP)_2$ MOF exhibited gravimetric capacitance of 116 F g^{-1} at 1 A g^{-1}, energy density of 4 W h kg^{-1} (at 0.5 kW kg^{-1}), and cyclic stability of 86% after 10 000 cycles.[35] In a recent report,[36] this HHTP linker was chemically modified with pendant aromatic amine groups, which was used to prepare Cu_3-$(HHTATP)_2$. This modification improved the energy density to ~9.3 W h kg^{-1}. Electrodes based on 2D-CMOFs of Ni HAB delivered a volumetric energy density of 20.7 W h L^{-1} at 0.74 kW L^{-1}.[5] The respective gravimetric energy density (at the same conditions/power) was 11.6 W h kg^{-1}, since the packing density of the electrode was ~1.8 g cm^{-3}. Although the volumetric capacitance was remarkably high (~600 F cm^{-3}), the practical performance metrics are primarily linked to the energy and power densities.[13] Even though such 2D-CMOFs are conductive, leveraging this key feature is hampered by the insulating interfaces between the MOF particles. For instance, in the case of highly conductive MXenes, conductive carbon additives are required to improve interfacial charge transfer,[4] allowing for a volumetric energy density of 18.5 W h L^{-1} at 0.24 kW L^{-1}. However, conductive additives can only randomly penetrate the interparticle space of the active material, their electrochemical activity is usually low and, most often, they lack functions for developing robust and covalent bridges with the active material particles.

We thus hypothesized that focusing on the chemical modification of the interfaces (rather than the linkers) would be crucial to develop seamless contacts between the 2D-CMOF particles towards full exploitation of their properties. For instance, Liu *et al.* prepared the $CoSe_2$/carbon composite with interfacial engineering.[37] A strong electric field generated at the interface allowed the fast electron transfer and ionic conductivity. The sample delivered 269.5 mA h g^{-1} of capacity at 5 A g^{-1} when used as an anode for sodium ion battery. To this end, we employed a structurally and chemically tailored conductive graphene derivative,[38,39] selectively functionalized with carboxylic groups (graphene acid, GA). The $Ni_3(HHTP)_2$ MOF (termed 2DNi) was synthesized *via* a facile, *in situ* growth on the surfaces of GA in water. Experimental results revealed the coordination between the metal nodes of 2DNi and the carboxyl groups from GA (Fig. 1a). This strategy substantially improved the electrochemical performance of the obtained 2DNiGA heterostructure, exceeding the improvement expected by a simple rule-of-mixtures combination of properties of individual components. The 2DNiGA electrode showed more than 100% capacitance improvement compared to electrodes synthesized under identical conditions using unfunctionalized pristine graphene or GA added post-synthesis *via* physical mixing. In the latter case no formation of coordination bonds with the nickel nodes of the MOF was observed, verifying our hypothesis on the importance of the interfacial bridges. A hybrid flexible supercapacitor (HSC, 2DNiGA//GA, Fig. 1a), employing 2DNiGA as a positive and GA as a negative electrode delivered top-rated gravimetric (71 W h kg^{-1} at 0.8 kW kg^{-1}), and volumetric (73.8 W h L^{-1} at 0.836 kW L^{-1}) energy density, keeping 41.6 W h L^{-1} at very high power of 9.36 kW L^{-1}. This performance surpassed previous MOF-based supercapacitors (Fig. 1b, c and Table S1†), such as 2D copper catecholate (Cu-CAT) MOF with 2.6 W h kg^{-1},[40] $Cu_3(HHTP)_2$ CMOF with 33 W h kg^{-1},[41] copper catecholate/polypyrrole hybrid[42] with an areal energy density of 22.4 μW h cm^{-2} (*versus* 213 μW h cm^{-2} for the 2DNiGA//GA), the nickel hexaaminobenzene (Ni-HAB) with a volumetric energy density of 20.7 W h L^{-1}.[5] Notably, it is also superior in the broader context of supercapacitor electrode materials, such as titanium carbides (Ti_3C_2) with 5.5 W h kg^{-1} and 18.5 W h L^{-1},[4] 3D graphene with 4.5 W h kg^{-1},[43] tri-composite of CNT/Graphene/PANI with 16.4 W h kg^{-1}, and 4 W h L^{-1},[17] and holey graphene with 35 W h kg^{-1} and 49 W h L^{-1}.[10] The 2DNiGA//GA is

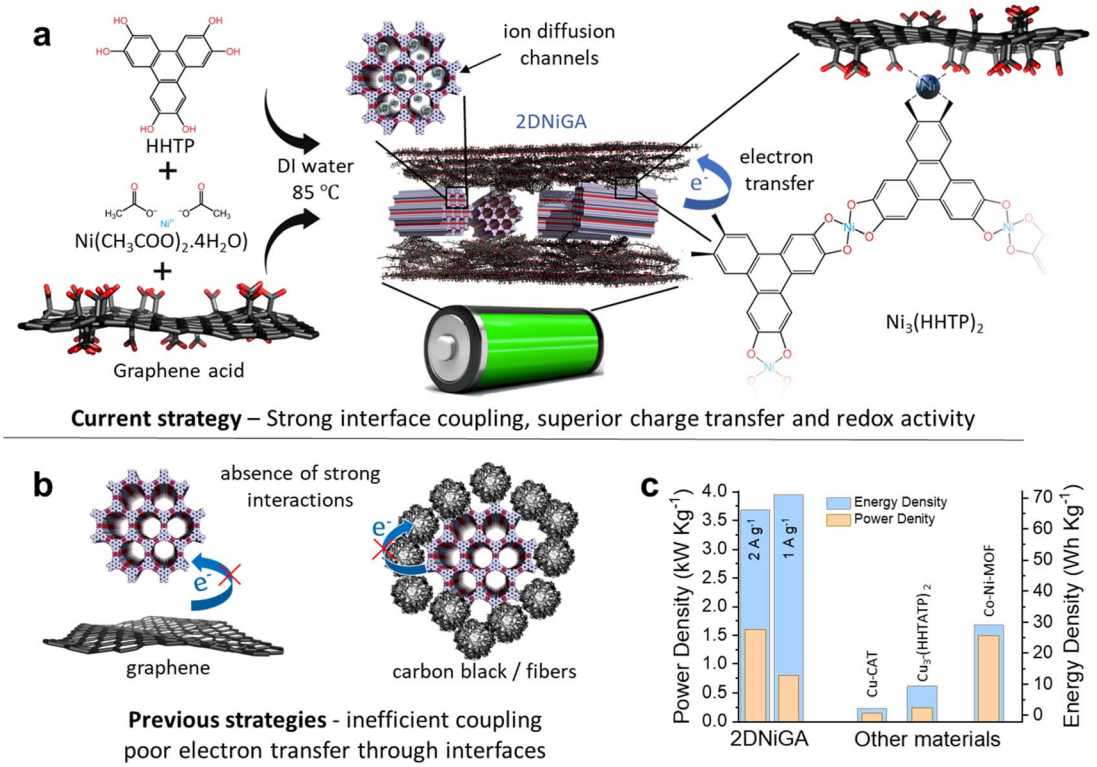

Fig. 1 (a) 2DNiGA synthesis resulting to covalent bonding between $Ni_3(HHTP)_2$ and GA at the molecular level. (b) Previous strategies for the development conducting channels between MOFs and conductive carbons. (c) Indicative comparision of energy density/power density with the previous MOFs: Cu-CAT,[40] $Cu_3(HHTATP)_2$,[36] and Co-Ni-MOF.[44]

also robust, retaining more than 94% of its performance after 10 000 charge/discharge cycles, or when bent at 180°. Moreover, after increasing the mass loading of the stack from 3 to 15 mg cm^{-2}, the HSC device retains its performance by 94.6%, further highlighting the role of seamless bridges for the design of future advanced materials for electrochemical energy storage.

2 Results and discussion

2.1 Physicochemical analysis

2DNi consists of stacked layers with hexagonal lattice that form through coordination between Ni ions and HHTP ligands. Leveraging GA as a functional and conductive nucleation solid support to grow 2DNi yields the hetero-structured 2DNiGA after simple mixing of the components and letting them react for 18 h at 85 °C (Fig. 1a). The presence of a large number of carboxylic groups allows the mass integration of conductive 2DNi with good interfacial and storing coupling which remains absent in the other strategies used in literature.[19,36,40] The mass content of GA in the 2DNiGA hybrid was ~41 wt%, according to thermogravimetric analyses (TGA) on GA, 2DNi, and 2DNiGA samples (Fig. S1,† and comments therein). Raman spectra (Fig. 2a) show the emergence of the graphene 2D band at 2680 cm^{-1} only in the case of the 2DNiGA and not in the GA, suggesting a less stacked layered structure for the 2DNiGA case than in the case of pristine GA. Previous experimental and theoretical studies showed the extensive hydrogen bonding and stacking of the pristine GA layers in the dried state, or in acidic conditions where the carboxyl groups are protonated.[39] However, the *in situ* growth of 2DNi CMOF crystals on the planes of GA appears to inhibit this stacking, leading to the emergence of the intense Raman 2D band.[45,46] Although such a symmetric 2D band can be observed in monolayer graphene and also in turbostratically arranged graphite,[45,46] in the present case, its absence in pristine GA and presence in 2DNiGA signals the existence of dissociated GA flakes in 2DNiGA. The XRD pattern of pristine 2DNi CMOF confirmed its crystallographic structure (Fig. S2†). The reflections in 2DNiGA corresponding to the 2DNi CMOF retain their positions as in the pristine CMOF, signaling the preservation of the CMOF structure. The notable decrease in MOF diffraction intensity in the XRD pattern of the composite is attributed to the nanoscale growth of MOF crystallites directly on the GA surface, which reduces long-range order and leads to peak broadening and suppression. Additionally, the high content of GA (~41 wt%) in the composite contributes to the lower overall signal from the MOF phase. Regarding the observed offset of the GA diffraction around 30.5°, this is due to the overlap of the graphene-related diffraction and the nearby diffraction of the 2DNi MOF, which appears at a slightly higher 2θ value. The formation of the 2DNiGA composite causes these two peaks to overlap and merge, resulting to an apparent shift in the observed position.

The FTIR analysis (Fig. 2b) revealed the CMOF bands due to the metal–oxygen bonds[47] at 690 cm^{-1} and in the range of 1400–

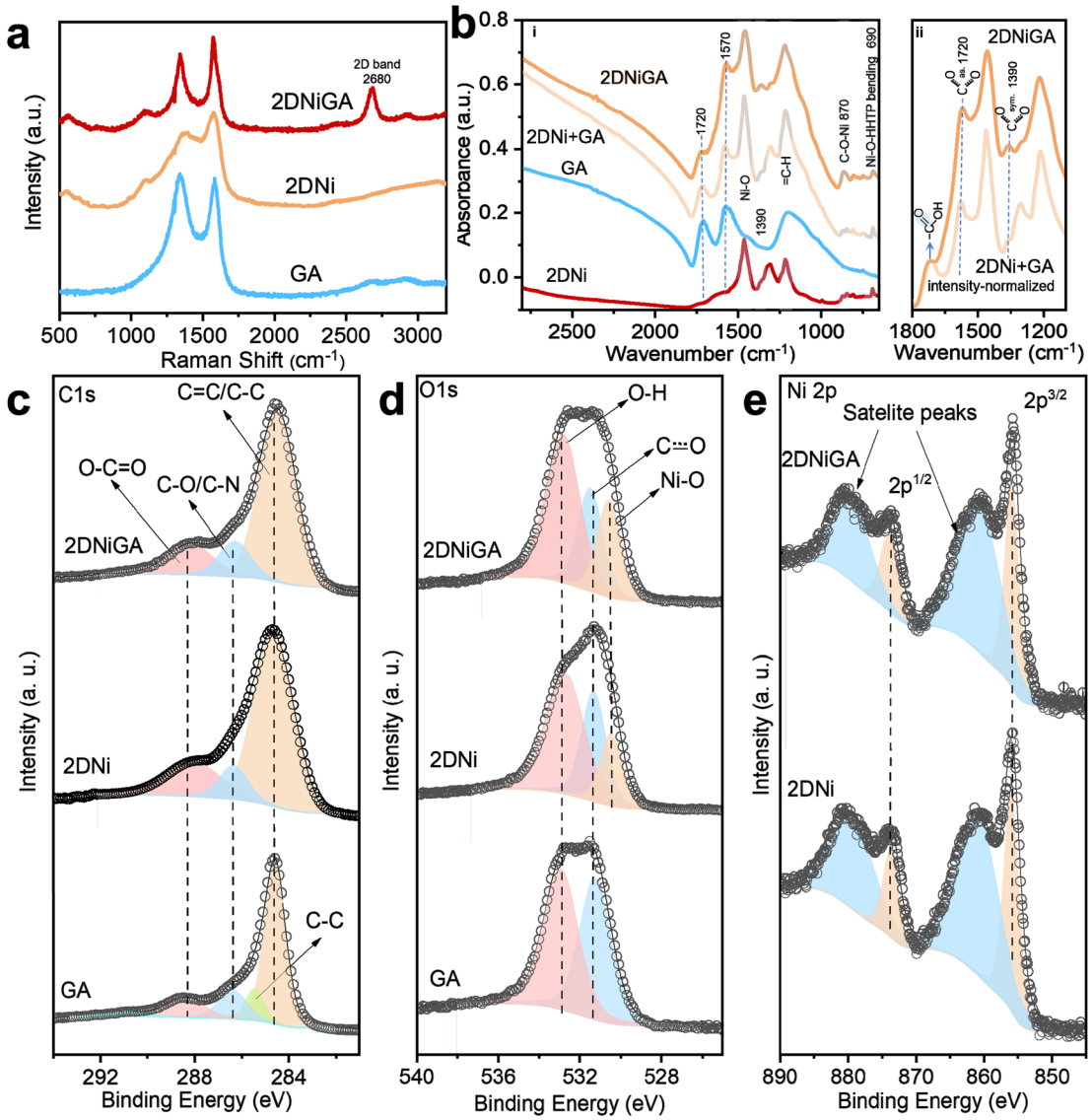

Fig. 2 Structural characterization of GA, 2DNi, and 2DNiGA composite: (a) Raman spectra comparison, (b) FTIR spectra comparison of GA, 2DNi, and 2DNiGA insitu composite with physical mixture of 2DNi + GA, XPS spectra comparison of GA, 2DNi and 2DNiGA, (c) C 1s, (d) O 1s, and (e) Ni 2p spectra comparison of 2DNi and 2DNiGA.

1500 cm^{-1} in the 2DNi and 2DNiGA samples. Most importantly, FTIR revealed the coordination of GA's carboxylic groups with the Ni metal ions of the CMOF (Fig. 2b i and ii). Specifically, the spectrum for the pristine GA exhibits a prominent carbonyl (C=O) stretching band at 1720 cm^{-1} of the carboxylic groups.[48,49] However, upon formation of the 2DNiGA composite, the carboxylic band intensity decreases, suggesting the formation of metal (Ni)-carboxylate complexes. The carboxylic-to-carboxylate transformation concurrently results in a marked increase in the intensity of the carboxylate antisymmetric and symmetric stretching vibrations, observed at ~1570 cm^{-1} and 1390 cm^{-1}, respectively. This behavior aligns with previously observed coordination of carboxylic graphene derivatives with metal ions.[50,51] To unequivocally prove the coordination of GA with the metal ions of the 2DNi CMOF, a simple physical mixture between 2DNi and GA (termed 2DNi + GA, Fig. 2b) was studied, where these carboxylate-Ni bands were much less pronounced, as deduced after normalization of the spectra using the 1720 cm^{-1} band for valid comparison (Fig. 2b ii). The coordination was further substantiated due to the changes in the 870 cm^{-1} band of the Ph-C–O-Ni bond in the MOF lattice.[52] This band has a notably higher intensity in the 2DNiGA composite, while in the case of the physical mixture (2DNi + GA) the band has the same footprint as in the pristine 2DNi. The difference is the co-presence of carboxylate-metal (O=C–O-Ni) type bonds in the 2DNiGA case, and only Ph-C–O-Ni type bonds in the pristine 2DNi and in the physical mixture. The carbon atom in the O=C–O–Ni bond belongs to carboxylate groups from GA, while in the Ph-C–O-Ni bond belongs to the benzene rings of the HHTP linker. Thus, the O=C–O-Ni bond has a higher dipole moment (*i.e.*, polarizability) because of the electron-withdrawing nature of the carbonyl group (C=O),

giving rise to the observed increased band intensity.[47,53] Overall, these findings indicate the successful covalent integration of GA with the 2DNi CMOF framework *via* the described metal–ligand coordination interactions.

The XPS analysis confirmed the expected chemical composition. The survey scan (Fig. S3†) confirmed the presence of Ni, C, and O elements in 2DNiGA. The C 1s XPS spectrum of 2DNiGA is deconvoluted into C=C/C–C, C–O/C–N, and O–C=O components at 284.5 eV, 286.3 eV, and 288.2 eV, respectively (Fig. 2c), which are well aligned with the C 1s spectra of pristine 2DNi, and GA. The GA O 1s spectrum (Fig. 2d) unveils CO and O–H components at 531.1 eV and 532.8 eV, respectively. The O 1s spectra of 2DNiGA and 2DNi are accompanied by an additional component at 530.5 eV corresponding to Ni-O.[54] The Ni 2p spectra (Fig. 2e) for 2DNi and 2DNiGA exhibit the Ni $2p_{3/2}$ and Ni $2p_{1/2}$ components at 855.6 eV and 873.6 eV, respectively, corresponding to the Ni^{2+} oxidation state.

The scanning electron microscopy (SEM) imaging on pristine 2DNi CMOF and the heterostructure with GA showed cylindrical rods ranging from 100 to 200 nm in length and from 30 to 50 nm in diameter (Fig. 3a), typical of the particular MOF. In the SEM of 2DNiGA product, the 2DNi CMOF is observed to intricately grow over the GA surface, forming a seamless heterostructure (Fig. 3b). Further, the cross-sectional SEM images of the 2DNiGA is given in Fig. S4,† showing the presence of the 2DNi rods around and between the GA sheets. The rods of the 2DNi CMOF in the product retain lengths of 100–200 nm, while diameters decrease to 10–20 nm. The densely covered GA flakes with the finely dispersed 2DNi CMOF rods and the absence of independent MOF rods highlight the initiation of the MOF growth from the nucleation sites on GA. The SEM of neat GA showed sheets of graphene flakes which exhibit densely stacked sheets (Fig. S5†), when compared to the 2DNiGA composite. TEM analysis on pristine 2DNi CMOF (Fig. 3c) and its heterostructure with GA (Fig. 3d) supported the observations from SEM. The SAED pattern of the 2DNi MOF showed the (100) plane of the MOF structure (inset of Fig. 3c). In the 2DNiGA (inset of Fig. 3d), the 2DNi CMOF nanorods are visibly accumulated over and within the surface of GA. The intercalation of 2DNi rods between GA sheets prevents its restacking and thus leads to the emergence of the 2D band in Raman spectra which is only visible in the case of 2DNiGA composite. As verified by FTIR spectroscopy, the GA surface, due to its carboxylic groups, offers nucleation sites for the 2DNi growth by coordinating the

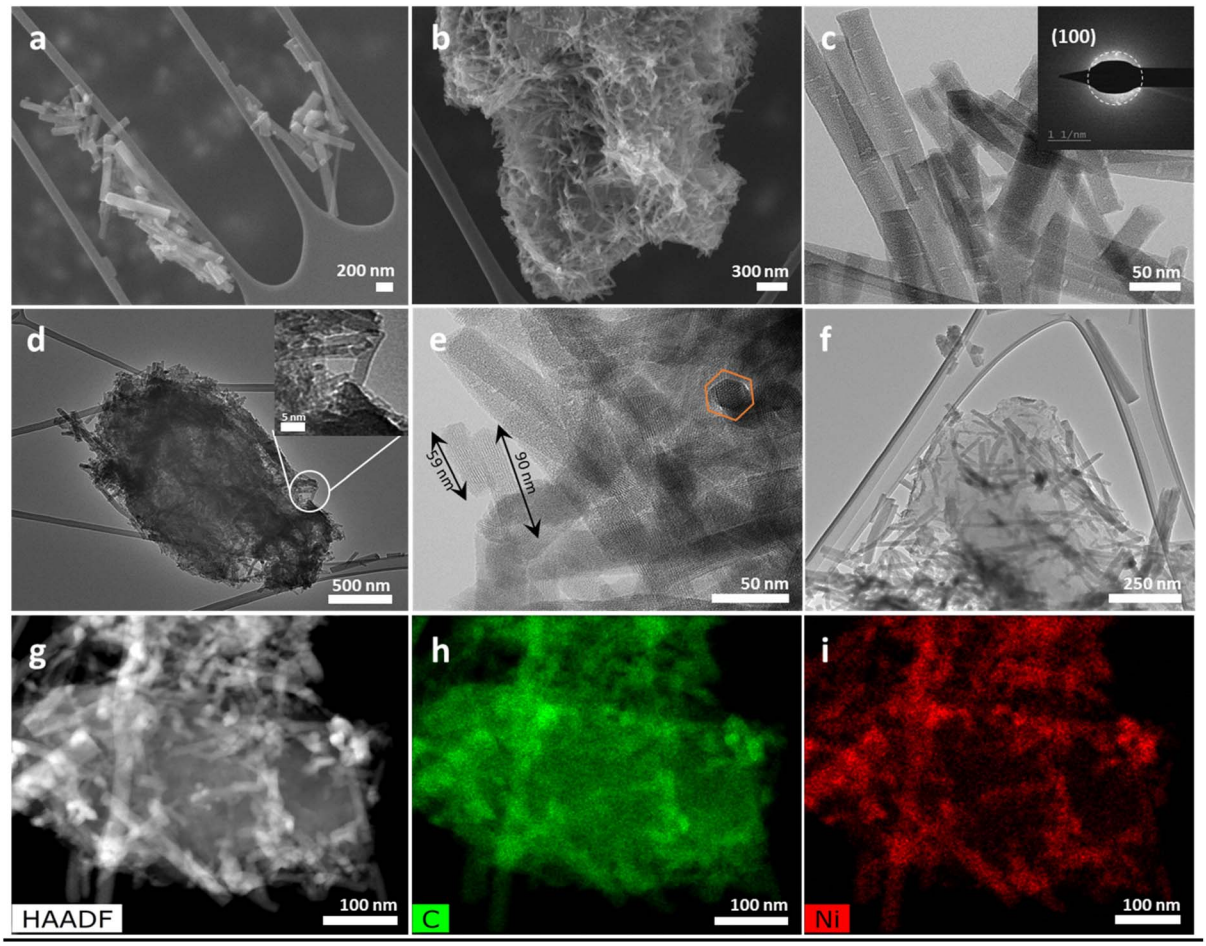

Fig. 3 (a) SEM of 2DNi, (b) SEM of 2DNiGA, (c) TEM of 2DNi (inset SAED), (d–e) TEM of 2DNiGA (inset of d: 2DNi rods attached to the GA sheets), (f) HRTEM of 2DNiGA, (g) HAADF-STEM image of 2DNiGA and the respective energy dispersive X-ray spectroscopy (EDXS) elemental mapping, for (h) carbon, (i) nickel.

Ni cations. The high magnification TEM image reveals the crystal planes of the 2DNi rods and the hexagonal pattern of the 2DNi rod cross-section (Fig. 3e). The distance calculated through the Fast Fourier Transform (FFT) analysis is 1.95 nm, which is in agreement with the XRD data ($2\theta = 5.5°$ of the (100) plane). The high-resolution TEM (HRTEM) further highlights the growth of the 2DNi rods over the GA surface (Fig. 3f). The energy-dispersive X-ray spectroscopy (EDS) analysis verified the XPS results regarding the elemental composition of the pristine 2DNi CMOF (Fig. S6a†) and the 2DNiGA heterostructure (Fig. S6b†). Elemental mapping with high-angle annular dark-field scanning transmission electron microscopy (HAADF-STEM) (Fig. 3g–i) showed the homogeneous carbon distribution (originating from GA) with higher intensity at the 2DNi MOF due to the organic linkers (Fig. 3h). Nickel, however, was selectively distributed in the sample coinciding with the spatial distribution of the 2DNi rods (Fig. 3i).

2.2 Electrochemical analysis in three-electrodes

To understand the charge storage properties of GA, 2DNi, and 2DNiGA products, three-electrode electrochemical measurements were performed in 1 M H_2SO_4 aqueous electrolyte between 0 and 1 V. The selection of the voltage window was based on the recorded current response from the CVs. As the voltage increased (Fig. S7†) above 1 V *vs.* Ag/AgCl the current also increased sharply, indicating water oxidation. Therefore, the potential window of 0 to 1 V *vs.* Ag/AgCl was selected as the most appropriate for the 2DNIGA electrode material. The 2DNiGA displayed a large CV area with intense redox peaks indicating higher electrochemical activity in comparison to pristine GA and 2DNi (Fig. 4a).[55] The redox peaks originate both from the redox activity of Ni ions present in the 2DNi CMOF structure,[56] but also from the GA (Fig. 4a). However, the higher intensity in the 2DNiGA heterostructure than in any of the individual components suggests a faster charge transport, boosting the expression of the redox events, and manifesting the effects of the covalent integration of GA (as FTIR results indicated), confirming the initial hypothesis. The redox peaks are reversible and observed even at high scan rates (Fig. S8a–c†), suggesting high rate capability and stability.[57]

GCD profiles at different current densities ranging from 0.5 to 10 A g^{-1} (Fig. S8d–f†) retained the redox-active profile of all the materials, as evident from the non-linear GCD patterns, between 0.3 to 0.6 V.[58] GCD at 1 A g^{-1} (Fig. 4b) verified the higher specific capacitance for the 2DNiGA composite (309 F g^{-1} at 1 A g^{-1}), followed by GA (269.7 F g^{-1}) and by the pristine 2DNi CMOF (223.6 F g^{-1}; capacitances were calculated according to the non-linear eqn S2†). All three electrode materials, 2DNiGA, GA, and 2DNi, exhibited excellent energy efficiency (EE) of approximately 100% across a wide range of current densities, indicating minimal internal resistance and efficient charge–discharge behavior. However, at the highest current density of 10 A g^{-1}, a slight deviation was observed. GA maintained the highest EE of 99.85%, likely due to its electric double-layer capacitance (EDLC)-dominated charge storage mechanism, which involves fast and reversible ion adsorption without significant faradaic losses. In contrast, 2DNi showed a drop in EE to 95%, which can be attributed to its pseudocapacitive redox behavior involving slower faradaic reactions that become less efficient at high current densities. The 2DNiGA composite retained an intermediate EE of 96.2%, suggesting that the covalent integration of GA with 2DNi effectively combines the fast kinetics of EDLC with the high-capacity redox features of the MOF, leading to a more balanced and efficient charge storage, even under high-rate conditions. For all three

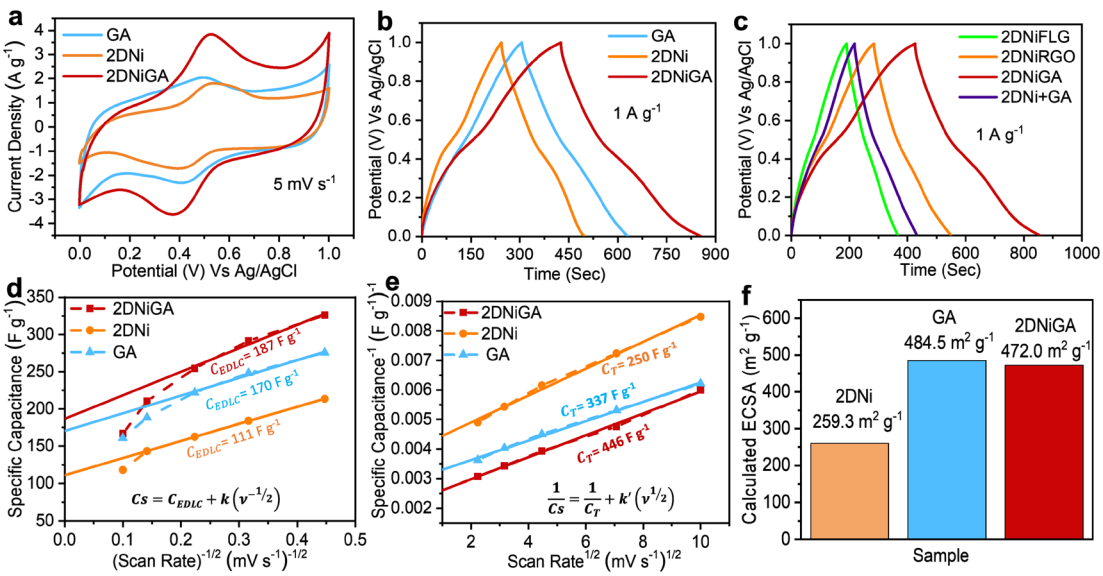

Fig. 4 Electrochemical analysis with three electrodes in 1 M H_2SO_4: (a) CVs of GA, 2DNi, and 2DNiGA at a scan rate of 5 mV s^{-1}, (b) GCD of GA, 2DNi, 2DNiGA at a current density of 1 A g^{-1}, (c) GCD of 2DNiGA compared with control samples of 2DNiRGO, 2DNiFLG, and 2DNi + GA at a current density of 1 A g^{-1}, Electrochemical kinetic studies of 2DNi, GA, and 2DNiGA electrodes: (d) variation of specific capacitance to $\nu^{-1/2}$ (ν: scan rate), (e) variation of inverse of the specific capacitance to $\nu^{1/2}$, and (f) electrochemical surface area calculations.

electrodes, the specific capacitance decreased with increasing current density or scan rate, which is a common feature of electrode materials and attributed to the insufficient time for electrolyte ions to access the pores of the electrodes (Fig. S9†).[59] Despite this, the 2DNiGA electrode retained a specific capacitance of 210.5 F g^{-1} even when the current density increased fivefold to 5 A g^{-1}.

To better demonstrate the role of the carboxylic functional groups of GA for the superior properties of 2DNiGA, control samples were also synthesized following the same procedure but using reduced graphene oxide (RGO) and few-layer graphene (FLG) instead of GA, affording the 2DNiRGO and 2DNiFLG samples. These materials displayed smaller CV areas than the 2DNiGA electrode (Fig. S10a†), particularly the FLG-based sample. The GCD curves (Fig. 4c) also revealed a substantially higher specific capacitance for 2DNiGA (309 F g^{-1}) than for 2DNiRGO (200.3 F g^{-1}) and 2DNiFLG (141.5 F g^{-1}) electrodes. Even the physical mixture between 2DNi and GA (2DNi + GA) showed a significantly lower specific capacitance of 169.3 F g^{-1}. The equivalent series resistance values determined from the Nyquist plots (Fig. S10b and c†) corroborated these results, indicating a very low resistance for 2DNiGA (0.54 Ω), almost half of those of 2DNiRGO (0.93 Ω), 2DNiFLG (1.07 Ω), and 2DNi + GA (0.86 Ω). These comparative results further confirmed the initial hypothesis about the crucial role of the covalent conjugation and bridging achieved between the 2DNi CMOF particles and the GA sheets in the 2DNiGA heterostructure, ascribing substantially improved performance. The performance was significantly inferior when the covalent interactions were absent (as in the physical 2DNi + GA mixture). The 2DNiRGO also had inferior properties (although synthesized in the same way as the 2DNiGA heterostructure), due to the miscellaneous and lower number of functional groups in RGO. The 2DNiFLG control sample with FLG lacking completely functional groups, was the least active material. Furthermore, the nearly 45-degree slope of the EIS line at the right of the Nyquist plot (low frequencies, Fig. S10b†) also indicates an ideal pseudocapacitive behavior of the 2DNiGA electrode. This confirms that the formation of covalent bridges increases the pseudocapacitive nature of the 2DNiGA electrode that was well evidenced by the prominent redox peaks in CV analysis (Fig. 4a) and non-linear GCD curves (Fig. 4b).

We conducted additional control experiments to study the effect of GA concentration on the electrochemical performance of the 2DNiGA composite (Fig. S11a†). While the optimized sample (1.5 mg mL^{-1} starting GA concentration) delivered a specific capacitance of 341 F g^{-1} at 0.5 A g^{-1}, the composites prepared with lower (1 mg mL^{-1}) and higher (2 mg mL^{-1}) starting GA concentrations showed significantly reduced capacitances of 103 F g^{-1} and 176 F g^{-1} at 0.5 A g^{-1}, respectively. The reduced performance at lower GA concentration (1 mg mL^{-1}) can be attributed to insufficient nucleation sites for the growth of 2DNi MOF and to fewer interfacial bridges. At higher GA concentration the reduced capacitance can be attributed to the loss of the balanced contribution of the redox-active components. Further, higher GA content can lead to restacking, hindering ion accessibility and disrupting charge transport pathways.

To further investigate the role of the metal center in the MOF structure, we synthesized two additional 2D MOF-GA composites with cobalt (2DCoGA) and copper (2DCuGA), while keeping the organic linker and the synthesis route unchanged. As shown in Fig. S11b,† the 2DCoGA composite delivered a specific capacitance of 254 F g^{-1} at 1 A g^{-1} (significantly lower than that of the original 2DNiGA material), whereas the 2DCuGA achieved 302 F g^{-1}, comparable to the 309 F g^{-1} of the original 2DNiGA material. The lower performance of 2DCoGA can be attributed to the less favorable redox behavior of cobalt in this specific MOF architecture, as evidenced by the absence of redox features in its discharge curve.

The above findings were further supported by the electrochemical kinetic studies, providing understanding about the properties of the 2DNiGA electrode, and quantitative insights on the electric double-layer capacitance (C_{EDLC}) and pseudocapacitance (C_{Pseudo}) contributions to the total theoretical capacitance (C_T).[60–62] C_{EDLC} was determined by the *y*-axis intercept of the specific capacitance (C_s) *versus* the reverse square root of scan rate ($\nu^{-1/2}$) plot ($C_s = C_{EDLC} + k\nu^{-1/2}$), while C_T was obtained by the intercept ($1/C_T$) of the $1/C_s$ *versus* $\nu^{1/2}$ plot ($1/C_s = 1/C_T + k\nu^{1/2}$) and *k* is constant. The C_{EDLC} values (Fig. 4d) of GA, 2DNi, and 2DNiGA were 170 F g^{-1}, 111 F g^{-1}, and 187 F g^{-1}, respectively. By subtracting the C_{EDLC} values from C_T (Fig. 4e), the C_{Pseudo} values were determined to be 167 F g^{-1}, 139 F g^{-1}, and 259 F g^{-1} for GA, 2DNi, and 2DNiGA electrodes, respectively. Thus, the C_{Pseudo}/C_{EDLC} ratio was 0.98, 1.25, and 1.39 for GA, 2DNi, and 2DNiGA, respectively, quantitatively indicating that the *in situ* incorporation of GA in 2DNi increases the pseudocapacitive character, in agreement with the previous analyses. The significant role of GA in the 2DNiGA heterostructure was also unveiled by the substantial increase in the electrochemical surface area (ECSA). The incorporation of 41 wt% GA led to an ECSA increase from 259.3 m^2 g^{-1} in 2DNi to 472 m^2 g^{-1} in 2DNiGA, demonstrating a marked enhancement in electrochemically active sites,[63] and corroborating the fast reaction kinetics (Fig. S12, 4f, eqn S3 and S4†).[64] This remarkable enhancement cannot simply be explained by the additive contribution of the individual ECSAs of the components. Notably, the composite attained an ECSA equivalent to pure GA, even though it contained only 41 wt% GA. This indicates a synergistic effect and emergence of new properties within the 2DNiGA heterostructure, where the presence of GA significantly amplified the electrochemical activity in the composite beyond what would be expected from the sum of its parts. The intricate properties in the 2DNiGA (covalent bridging, improved GA exfoliation), leading to superior electrochemical behavior, render it very promising and, probably, more advantageous than many state-of-the-art electrode materials for supercapacitors, as documented in detail in Table S1.† In some cases, the metrics according to three-electrode measurements show high three-electrode capacitances (entries #1, 7, 8, 12, 14, 15, 16), but in these cases, the voltage is small, leading (as later discussed about the full-cell metrics) to low energy densities.

The 2DNiGA heterostructure was utilized as a positive electrode material (0 to 1 V) in hybrid supercapacitors (HSC). After testing several carbons, pristine GA was selected as a counter electrode in the negative potential window from −0.6 to 0 V for the construction of the HSC. Therefore, the HSC was assembled within the operating potential window of 0 to 1.6 V after mass balancing (Fig. 5a) using eqn S6.† The total mass loading in 2DNiGA//GA HSC was 3 mg cm^{-2} and the total density calculated by considering the active material thickness of both electrodes was 1.04 g cm^{-3} (used to calculate the volumetric performance). The CV curves at different scan rates (Fig. 5b) indicated a quasi-rectangular behavior, persistent at all scan rates, while GCD analysis at current densities ranging from 1 to 10 A g^{-1} (Fig. 5c) derived a specific capacitance of about 200 F g^{-1} for the HSC device at 1 A g^{-1} (eqn S7†), which was only reduced to 146.8 F g^{-1} at 5 A g^{-1} (Fig. 5d). EIS measurements and Nyquist plots derived the equivalent series resistance (R_s) and the charge transfer resistance (R_{ct}) of the device.[65] Remarkably, the R_s value was 3.4 Ω, while the absence of a semicircle in the high-frequency region indicated a very low R_{ct} and the minimal impedance encountered across the electrode/electrolyte interface.[66] The lower resistance in the 2DNiGA//GA HSC device facilitates rapid charge transport, (Fig. S13†), also corroborating the previous observations.

The energy and power densities of supercapacitors are key metrics for their evaluation. The Ragone plot (Fig. 6a) of the HSC device shows that, at 1 A g^{-1}, the 2DNiGA//GA HSC achieved an ultrahigh gravimetric energy density of 71 W h kg^{-1} at a power density of 800 W kg^{-1}. Even at the very high power density of 9 kW kg^{-1}, the device retained an energy density of 40 W h kg^{-1}. The performance in volumetric terms is another critically important metric in the modern landscape of portable energy storage technologies, as systems displaying both high gravimetric and volumetric energies are particularly challenging to design.[5,33,67,68] The HSC device delivered a volumetric capacitance of 208 F cm^{-3} at a current density of 1 A g^{-1} (or 3 mA cm^{-2}; eqn S9†). Accordingly, the highest volumetric energy density was 73.8 W h L^{-1} at a power of 836 W L^{-1}. At higher current rates, even when the power density jumped to 9.36 kW L^{-1}, the volumetric energy density was retained as high as 41.6 W h L^{-1}. The long-term cycling stability of the device was evaluated for 10 000 continuous charge–discharge cycles, retaining 96.1% of its specific capacitance, along with high coulombic efficiency of 98.2% (Fig. 6b). To present these results in the context of the state of the art, Table S1†, Fig. 6c and d provide detailed comparisons with top-performing systems. In terms of full devices (*i.e.*, two-electrode systems) the 2DNiGA//GA HSC is superior regarding the key metrics of gravimetric energy and power density (Fig. 6c), but also regarding the volumetric terms (Fig. 6d). These comparisons underscore the outstanding performance of the 2DNiGA//GA

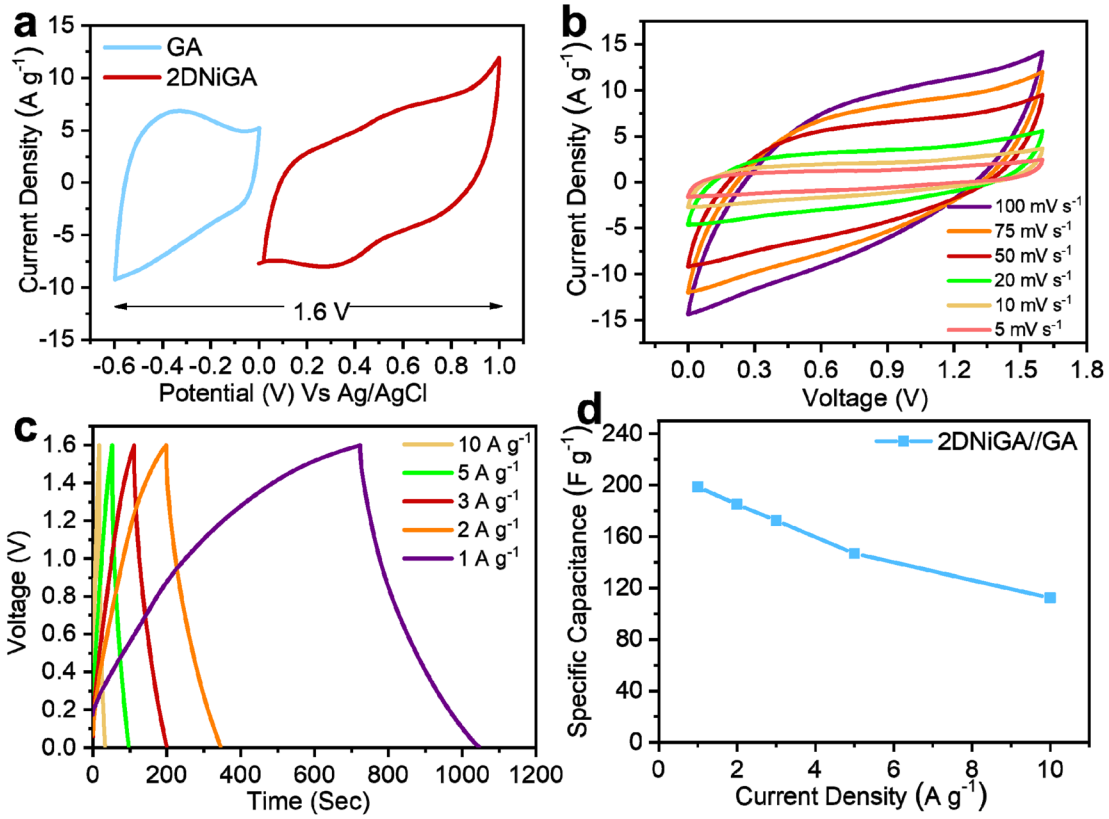

Fig. 5 Electrochemical analysis of 2DNiGA//GA HSC device: (a) CV optimization of HSC device, (b) CV at different scan rates, (c) GCD at different current densities, (d) variation of gravimetric capacitance *vs.* current density.

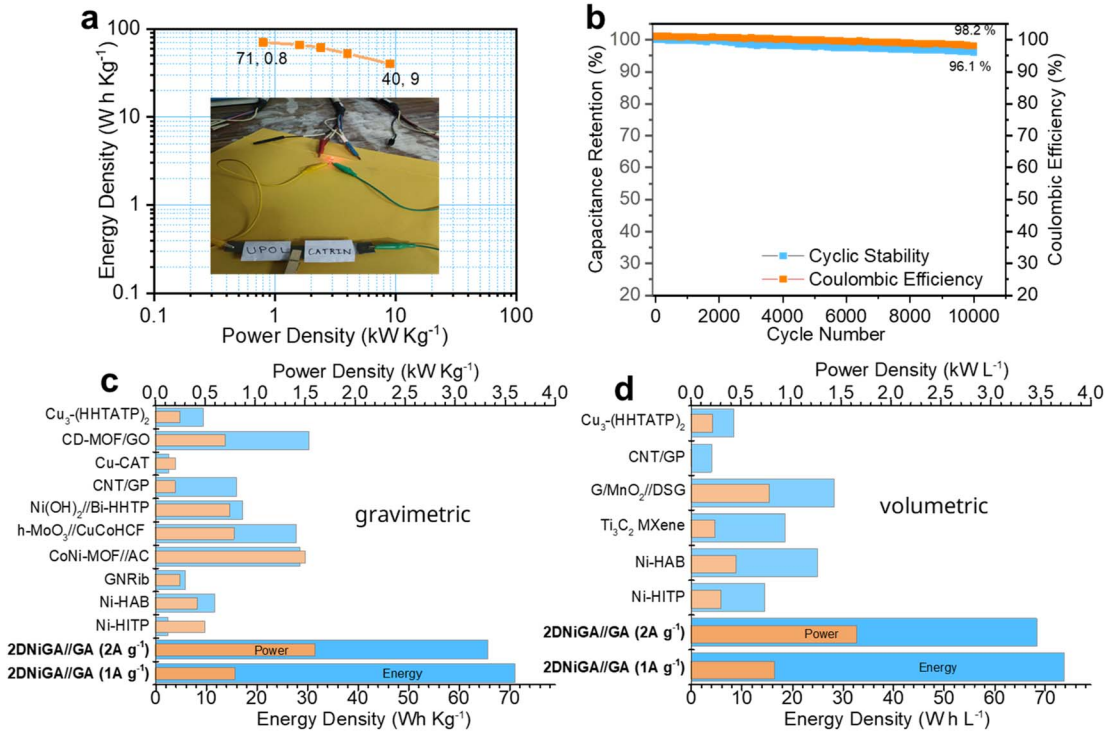

Fig. 6 Electrochemical analysis of 2DNiGA//GA HSC Device: (a) Ragone plot (inset shows a red LED lamp operating using the HSC device), (b) cyclic stability and coulombic efficiency test after 10 000 cycles, the energy and power density output achieved by the 2DNiGA//GA HSC device compared to symmetric and asymmetric supercapacitor devices from literature with respect to (b) gravimetric terms, and (c) in volumetric terms. Key to the material abbreviations: CD-MOF/GO: cyclodextrin MOF induced graphene oxide (Adv. Sci.[19]); Cu-CAT: copper catecholate (Adv. Fun. Mater.[40]); CNT/GP: carbon nanotubes/graphene petals (Nat. Commun.[17]); Cu_3-(HHTATP)$_2$: Cu- 2,3,6,7,10,11-hexahydroxy-1,5,9-triamino-triphenylene (J. Am. Chem. Soc.[36]); $Ni(OH)_2$/Bi-HHTP: Nickel hydroxide and 2D bismuth CMOF asymmetric supercapacitor (Dalton Trans.[69]); h-MoO_3//CuCoHCF: hexagonal molybdenum oxide and multimetallic Prussian blue analogue asymmetric supercapacitor (Nat. Commun.[70]); CoNi-MOF//AC: oriented cobalt-nickel MOF on carbon fiber paper and activated carbon asymmetric supercapacitor (Adv. Energy Mater.[44]); GNRib: MOF derived graphene nanoribbons (Nature. Chem[18]); Ni-HAB: 2D Nickel HAB CMOF (Nature Energy[5]); Ni-HITP: 2D Nickel-HITP CMOF (Nature Mater.[33]); G/MnO_2//DSG: graphene/manganese dioxide compoiste and 3D densely stacked graphene incorporated asymmetric supercapacitor (Small[71]); Ti_3C_2 MXene: titanium carbide MXene (Science[4]).

HSC, surpassing not only MOF-based supercapacitors but also advanced carbon-based and hybrid systems.

The device fully retained its properties when tested at different bending angles (Fig. S14†). Upon bending the HSC device from 0° to 30°, 60°, 90°, 135°, and 180°, and back, the CV curves at 50 mV s^{-1} remain unchanged, confirming the electrodes' stability and suitability for flexible, wearable energy storage applications. Another crucial feature regarding the applicability of electrode materials is related to their performance under high mass loading.[11,72] After increasing the mass

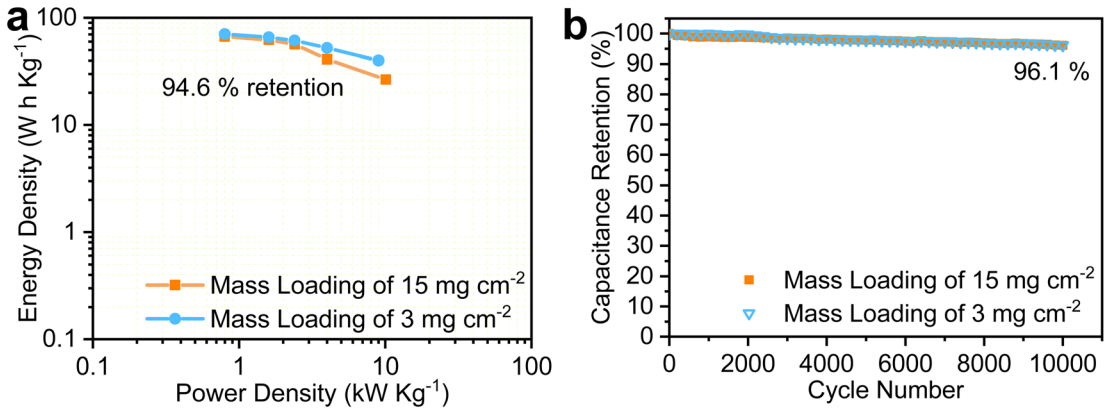

Fig. 7 High and low mass loading tests of the 2DNiGA//GA 1.6 V HSC device: (a) Ragone plot, and (b) cyclic stability comparison.

loading five times (*i.e.*, to 15 mg cm^{-2}) 94.6% of the energy density was retained (Fig. 7a). Similarly, the HSC device displayed high stability, keeping 96.1% of its capacitance after 10 000 cycles (Fig. 7b).

The high electrochemical performance of the 2DNiGA material and the 2DNiGA//GA HSC is ascribed to the effective chemical modification of the interfaces between the 2D CMOF and the conductive additive (the functionalized graphene, Fig. 1), which enhances charge transport and overall conductivity. These features result in pronounced pseudocapacitive behavior, as evidenced by the redox peaks in CVs, by the electrochemical impedance spectroscopy, and by the quantitative kinetic analysis.

3 Conclusions

A two-dimensional conductive and porous nickel organic framework (2DNi CMOF) is integrated *via* conductive covalent bridges with GA, a densely and selectively carboxyl functionalized graphene, which develops coordination bonds between GA's carboxylic groups and the nickel nodes of the 2DNi CMOF. This seamless integration occurs during the *in situ* growth of the CMOF in the presence of GA. These interactions prevent restacking of GA layers in the 2DNiGA heterostructure, as evidenced by the appearance of the 2D Raman band. This synergy leads to significant enhancement in electrochemical performance, beyond what would be expected from a simple combination of the individual components. Specifically, the conductive bridges and exfoliation enhance charge transfer, as impedance measurements revealed, promoting redox activity, pseudocapacitance, and increased electrochemical surface area. Proper mass balancing in an asymmetric supercapacitor—using 2DNiGA as the positive and GA as the negative electrode—results in excellent energy storage capacity, long cycle life, and fast charge/discharge rates, even at high mass loadings. Importantly the asymmetric device simultaneously achieves superior gravimetric and volumetric energy densities, which are key metrics for practical supercapacitors. This study lays the groundwork for overcoming interparticle insulation in conductive 2D MOFs through advanced integration with functional graphene derivatives, enabling high-performance energy storage in next-generation supercapacitors.

Data availability

The data that support the findings of this study are openly available in Zenodo record **https://zenodo.org/records/15312091**.

Author contributions

S.·S.: experimental, analysis, writing – original draft, methodology, investigation, visualization, funding acquisition; V. S.: writing original draft, data analysis; P. D.: analysis, discussion; Mansi.: electrochemical kinetics studies and analysis; V.·K.: control experiments and electrochemical analysis; M. K.: data analysis, discussion; A. C.·P.: data analysis, discussion, visualization; R. Z.: supervision, funding acquisition, review & editing; A. B.: supervision, funding acquisition, visualization, writing original draft, review, and editing.

Conflicts of interest

The authors declare no competing financial interest.

Acknowledgements

S. Sundriyal acknowledges the support from the European Union's Horizon 2020 research and innovation programme under the Marie Skłodowska-Curie grant agreement No. 101065296. V. Shrivastav acknowledges the support from the European Union's Horizon 2020 research and innovation programme under the Marie Skłodowska-Curie grant agreement No. 101107732. M. Khandelwal acknowledges the support from the European Union's Horizon 2020 research and innovation programme under the Marie Skłodowska-Curie grant agreement No. 101180679. Funded by the European Union. Views and opinions expressed are however those of the author(s) only and do not necessarily reflect those of the European Union or European Commission. Neither the European Union nor the granting authority can be held responsible for them. A. Bakandritsos acknowledges support from the Czech Science Foundation (grant no. 22-27973K). The work is also supported from the ERDF/ESF project TECHSCALE (No. CZ.02.01.01/00/22_008/0004587), and from the European Union under the REFRESH – Research Excellence for Region Sustainability and High-tech Industries (CZ.10.03.01/00/22_003/0000048) *via* the Operational Programme Just Transition. We thank Jiri Hosek and Dr Eirini Ioannou for SEM, Emil Remeslnicek for TGA, Jana Straska for TEM, Ondrej Tomanec for HR-TEM, and Dr Josef Kaslik for XRD.

References

1 D. Larcher and J.-M. Tarascon, *Nat. Chem.*, 2015, **7**, 19–29.
2 J. W. Choi and D. Aurbach, *Nat. Rev. Mater.*, 2016, **1**, 16013.
3 Z. Li, S. Gadipelli, H. Li, C. A. Howard, D. J. L. Brett, P. R. Shearing, Z. Guo, I. P. Parkin and F. Li, *Nat. Energy*, 2020, **5**, 160–168.
4 M. R. Lukatskaya, O. Mashtalir, C. E. Ren, Y. Dall'Agnese, P. Rozier, P. L. Taberna, M. Naguib, P. Simon, M. W. Barsoum and Y. Gogotsi, *Science*, 2013, **341**, 1502–1505.
5 D. Feng, T. Lei, M. R. Lukatskaya, J. Park, Z. Huang, M. Lee, L. Shaw, S. Chen, A. A. Yakovenko, A. Kulkarni, J. Xiao, K. Fredrickson, J. B. Tok, X. Zou, Y. Cui and Z. Bao, *Nat. Energy*, 2018, **3**, 30–36.
6 Q. Wang, J. Yan and Z. Fan, *Energy Environ. Sci.*, 2016, **9**, 729–762.
7 D. Yu, K. Goh, H. Wang, L. Wei, W. Jiang, Q. Zhang, L. Dai and Y. Chen, *Nat. Nanotechnol.*, 2014, **9**, 555–562.
8 Y. Zhu, S. Murali, M. D. Stoller, K. J. Ganesh, W. Cai, P. J. Ferreira, A. Pirkle, R. M. Wallace, K. A. Cychosz,

M. Thommes, D. Su, E. A. Stach and R. S. Ruoff, *Science*, 2011, **332**, 1537–1541.
9 X. Yang, C. Cheng, Y. Wang, L. Qiu and D. Li, *Science*, 2013, **341**, 534–537.
10 Y. Xu, Z. Lin, X. Zhong, X. Huang, N. O. Weiss, Y. Huang and X. Duan, *Nat. Commun.*, 2014, **5**, 4554.
11 H. Li, Y. Tao, X. Zheng, J. Luo, F. Kang, H.-M. Cheng and Q.-H. Yang, *Energy Environ. Sci.*, 2016, **9**, 3135–3142.
12 V. Šedajová, A. Bakandritsos, P. Błoński, M. Medveď, R. Langer, D. Zaoralová, J. Ugolotti, J. Dzíbelová, P. Jakubec, V. Kupka and M. Otyepka, *Energy Environ. Sci.*, 2022, **15**, 740–748.
13 P. Simon and Y. Gogotsi, *Nat. Mater.*, 2008, **7**, 845–854.
14 E. Pomerantseva, F. Bonaccorso, X. Feng, Y. Cui and Y. Gogotsi, *Science*, 2019, **366**, eaan8285.
15 Y. A. Kumar, G. R. Reddy, T. Ramachandran, D. K. Kulurumotlakatla, H. S. M. Abd-Rabboh, A. A. Abdel Hafez, S. S. Rao and S. W. Joo, *J. Energy Storage*, 2024, **80**, 110303.
16 T. Lin, I.-W. Chen, F. Liu, C. Yang, H. Bi, F. Xu and F. Huang, *Science*, 2015, **350**, 1508–1513.
17 G. Xiong, P. He, Z. Lyu, T. Chen, B. Huang, L. Chen and T. S. Fisher, *Nat. Commun.*, 2018, **9**, 790.
18 P. Pachfule, D. Shinde, M. Majumder and Q. Xu, *Nat. Chem.*, 2016, **8**, 718–724.
19 W. Zhang, Z. Zheng, L. Lin, X. Zhang, M. Bae, J. Lee, J. Xie, G. Diao, H. Im, Y. Piao and H. Pang, *Adv. Sci.*, 2023, **10**, 2304062.
20 Q. Li, Z. Dai, J. Wu, W. Liu, T. Di, R. Jiang, X. Zheng, W. Wang, X. Ji, P. Li, Z. Xu, X. Qu, Z. Xu and J. Zhou, *Adv. Energy Mater.*, 2020, **10**, 1903750.
21 S. Sundriyal, H. Kaur, S. K. Bhardwaj, S. Mishra, K.-H. Kim and A. Deep, *Coord. Chem. Rev.*, 2018, **369**, 15–38.
22 R. Du, Y. Wu, Y. Yang, T. Zhai, T. Zhou, Q. Shang, L. Zhu, C. Shang and Z. Guo, *Adv. Energy Mater.*, 2021, **11**, 2100154.
23 Y. A. Kumar, S. Vignesh, T. Ramachandran, K. D. Kumar, A. G. Al-Sehemi, M. Moniruzzaman and T. H. Oh, *J. Energy Storage*, 2024, **97**, 112826.
24 W. Liu, Y. Zhao, J. Zheng, D. Jin, Y. Wang, J. Lian, S. Yang, G. Li, Y. Bu and F. Qiao, *J. Colloid Interface Sci.*, 2022, **606**, 728–735.
25 Y. Zhao, S. Wang, F. Ye, W. Liu, J. Lian, G. Li, H. Wang, L. Hu and L. Wu, *J. Mater. Chem. A*, 2022, **10**, 16212–16223.
26 N. Cherupurakal, R. Krishnapriya, A. Bojarajan, T. Ramachandran, S. Sangaraju, M. S. Mozumder and A.-H. I. Mourad, *Mater. Renew. Sustain. Energy*, 2024, **13**, 361–373.
27 J.-Z. Hu, W.-J. Liu, J.-H. Zheng, G.-C. Li, Y.-F. Bu, F. Qiao, J.-B. Lian and Y. Zhao, *Rare Met.*, 2023, **42**, 916–928.
28 J. Han, H. Xu, B. Zhao, R. Sun, G. Chen, T. Wu, G. Zhong, Y. Gao, S. L. Zhang, Y. Yamauchi and B. Guan, *J. Am. Chem. Soc.*, 2024, **146**, 18979–18988.
29 G. Xu, C. Zhu and G. Gao, *Small*, 2022, **18**, 2203140.
30 L. S. Xie, G. Skorupskii and M. Dincă, *Chem. Rev.*, 2020, **120**, 8536–8580.
31 X. Deng, J.-Y. Hu, J. Luo, W.-M. Liao and J. He, *Top. Curr. Chem.*, 2020, **378**, 27.
32 T.-H. Chen, I. Popov, W. Kaveevivitchai and O. Š. Miljanić, *Chem. Mater.*, 2014, **26**, 4322–4325.
33 D. Sheberla, J. C. Bachman, J. S. Elias, C.-J. Sun, Y. Shao-Horn and M. Dincă, *Nat. Mater.*, 2017, **16**, 220–224.
34 S. Bi, H. Banda, M. Chen, L. Niu, M. Chen, T. Wu, J. Wang, R. Wang, J. Feng, T. Chen, M. Dincă, A. A. Kornyshev and G. Feng, *Nat. Mater.*, 2020, **19**, 552–558.
35 J. W. Gittins, C. J. Balhatchet, Y. Chen, C. Liu, D. G. Madden, S. Britto, M. J. Golomb, A. Walsh, D. Fairen-Jimenez, S. E. Dutton and A. C. Forse, *J. Mater. Chem. A*, 2021, **9**, 16006–16015.
36 G. Lee, G. Park and S. S. Park, *J. Am. Chem. Soc.*, 2024, **146**, 29767–29772.
37 X. Liu, D. Xue, R. Ren, T. Ou, T. Sun, Y. Han, F. Jin, Y. Li, Y. Zhao and J. Zhang, *Chem. Eng. J.*, 2024, **496**, 153790.
38 A. Bakandritsos, P. Jakubec, M. Pykal and M. Otyepka, *FlatChem*, 2019, **13**, 25–33.
39 A. Bakandritsos, M. Pykal, P. Błoński, P. Jakubec, D. D. Chronopoulos, K. Poláková, V. Georgakilas, K. Čépe, O. Tomanec, V. Ranc, A. B. Bourlinos, R. Zbořil and M. Otyepka, *ACS Nano*, 2017, **11**, 2982–2991.
40 W. Li, K. Ding, H. Tian, M. Yao, B. Nath, W. Deng, Y. Wang and G. Xu, *Adv. Funct. Mater.*, 2017, **27**, 1702067.
41 M. Shaheen, M. Z. Iqbal, S. Siddique, S. Aftab and S. M. Wabaidur, *Mater. Today Sustain.*, 2023, **23**, 100415.
42 R. Hou, M. Miao, Q. Wang, T. Yue, H. Liu, H. S. Park, K. Qi and B. Y. Xia, *Adv. Energy Mater.*, 2020, **10**, 1901892.
43 X. Wang, Y. Zhang, C. Zhi, X. Wang, D. Tang, Y. Xu, Q. Weng, X. Jiang, M. Mitome, D. Golberg and Y. Bando, *Nat. Commun.*, 2013, **4**, 2905.
44 T. Deng, Y. Lu, W. Zhang, M. Sui, X. Shi, D. Wang and W. Zheng, *Adv. Energy Mater.*, 2018, **8**, 1702294.
45 L. M. Malard, M. A. Pimenta, G. Dresselhaus and M. S. Dresselhaus, *Phys. Rep.*, 2009, **473**, 51–87.
46 A. C. Ferrari, *Solid State Commun.*, 2007, **143**, 47–57.
47 J. Liu, Z. Chen, H. Liu, S. Qin, M. Li, L. Shi, C. Zhou, T. Liao, C. Li, Q. Lv, M. Liu, M. Zou, Y. Deng, Z. Wang and L. Wang, *Small*, 2024, **20**, 2305076.
48 Z. Çiplak, N. Yildiz and A. Çalimli, *Fullerenes, Nanotubes Carbon Nanostruct.*, 2015, **23**, 361–370.
49 N. K. Sudesh, S. Das, C. Bernhard and G. D. Varma, *Supercond. Sci. Technol.*, 2013, **26**, 095008.
50 J. Oomens and J. D. Steill, *J. Phys. Chem. A*, 2008, **112**, 3281–3283.
51 K. I. Hadjiivanov, D. A. Panayotov, M. Y. Mihaylov, E. Z. Ivanova, K. K. Chakarova, S. M. Andonova and N. L. Drenchev, *Chem. Rev.*, 2021, **121**, 1286–1424.
52 A. Saadi, K. Lanasri, K. Bachari, D. Halliche and C. Rabia, *Open J. Phys. Chem.*, 2012, **02**, 73–80.
53 C. Guo, Z. Li, F. Duan, Z. Zhang, F. Marchetti and M. Du, *J. Mater. Chem. B*, 2020, **8**, 9951–9960.
54 T. Kou, M. Chen, F. Wu, T. J. Smart, S. Wang, Y. Wu, Y. Zhang, S. Li, S. Lall, Z. Zhang, Y.-S. Liu, J. Guo, G. Wang, Y. Ping and Y. Li, *Nat. Commun.*, 2020, **11**, 590.
55 D. Voiry, M. Chhowalla, Y. Gogotsi, N. A. Kotov, Y. Li, R. M. Penner, R. E. Schaak and P. S. Weiss, *ACS Nano*, 2018, **12**, 9635–9638.

56 J. Yang, P. Xiong, C. Zheng, H. Qiu and M. Wei, *J. Mater. Chem. A*, 2014, **2**, 16640–16644.
57 M. F. El-Kady, V. Strong, S. Dubin and R. B. Kaner, *Science*, 2012, **335**, 1326–1330.
58 L.-Q. Mai, A. Minhas-Khan, X. Tian, K. M. Hercule, Y.-L. Zhao, X. Lin and X. Xu, *Nat. Commun.*, 2013, **4**, 2923.
59 M. Majumder, M. S. Santosh, R. Viswanatha, A. K. Thakur, D. P. Dubal and K. Jayaramulu, *Energy Storage Mater.*, 2021, **37**, 396–416.
60 D. Mohanadas, M. A. A. Mohd Abdah, N. H. N. Azman, T. B. S. A. Ravoof and Y. Sulaiman, *Sci. Rep.*, 2021, **11**, 11747.
61 V. Shrivastav, S. Sundriyal, U. K. Tiwari, K.-H. Kim and A. Deep, *Energy*, 2021, **235**, 121351.
62 S. Ardizzone, G. Fregonara and S. Trasatti, *Electrochim. Acta*, 1990, **35**, 263–267.
63 E. Cossar, M. S. E. Houache, Z. Zhang and E. A. Baranova, *J. Electroanal. Chem.*, 2020, **870**, 114246.
64 Y. Yoon, B. Yan and Y. Surendranath, *J. Am. Chem. Soc.*, 2018, **140**, 2397–2400.
65 B.-A. Mei, O. Munteshari, J. Lau, B. Dunn and L. Pilon, *J. Phys. Chem. C*, 2018, **122**, 194–206.
66 J. Huang, Z. Li, B. Y. Liaw and J. Zhang, *J. Power Sources*, 2016, **309**, 82–98.
67 Y. Gogotsi and P. Simon, *Science*, 2011, **334**, 917–918.
68 W. Gu and G. Yushin, *WIREs Energy Environ.*, 2014, **3**, 424–473.
69 S. Chen, H. Zhang, X. Li, Y. Liu, M. Zhang, X. Gao, X. Chang, X. Pu and C. He, *Dalton Trans.*, 2023, **52**, 4826–4834.
70 T. Xu, Z. Xu, T. Yao, M. Zhang, D. Chen, X. Zhang and L. Shen, *Nat. Commun.*, 2023, **14**, 8360.
71 L. Sheng, L. Jiang, T. Wei and Z. Fan, *Small*, 2016, **12**, 5217–5227.
72 W. Guo, C. Yu, S. Li and J. Qiu, *Energy Environ. Sci.*, 2021, **14**, 576–601.

